Single-Step Preparation of Oxide−Oxide Nanocomposites: Chemical Vapor Synthesis of $LnAlO_3/Al_2O_3$ (Ln = Pr, Nd) Thin Films

Michael Veith,[†] Sanjay Mathur,*[,†] Hao Shen,[‡] Nicolas Lecerf,[†] Stefan Hüfner,[‡] and Mohammad H. Jilavi[§]

Institute of Inorganic Chemistry, Institute of Experimental Physics, and Institute of New Materials, Saarland University, D-66041 Saarbruecken, Germany

Received March 20, 2001. Revised Manuscript Received June 20, 2001

Thin films containing nanometer-sized $PrAlO_3$ or $NdAlO_3$ crystals evenly dispersed in an amorphous Al_2O_3 matrix were grown by chemical vapor deposition (CVD) of heterometal alkoxides, $[Ln\{Al(OPr^i)_4\}_3(Pr^iOH)]$ (Ln = Pr (**1**), Nd (**2**)). The lanthanoid to aluminum ratio in the precursors, established by single-crystal X-ray diffraction and chemical analyses of the crystalline products, enables the formation of a stoichiometric 1:1 composite of the general formula $LnAlO_3/Al_2O_3$ in a *single-stage* synthesis. The gas-phase thermolysis of **1** and **2** in a cold-wall reactor gave amorphous films of formal composition $LnAl_3O_6$, suggesting intact vaporization and decomposition of the heterometal frameworks on the substrates. On-line mass spectral analysis of the gaseous products formed during the CVD process revealed isopropyl alcohol, acetone, propene, and dihydrogen as the main byproducts. The electron spectroscopy for chemical analysis and energy-dispersive X-ray analysis confirmed the film compositions to be $LnAl_3O_6$, which was shown to be homogeneous through the film bulk by glow discharge mass spectrometry. The surface imaging (scanning electron microscopy/atomic force microscopy) exhibits films with a regular globulated morphology. The annealing of as-deposited films at 800 °C shows $PrAlO_3$ and $NdAlO_3$ to be the only crystalline phases (X-ray diffraction) with average grain sizes of 14 and 12 nm, respectively. The residual Al component (Al_2O_3) remains amorphous until 1200 °C; however, the evolution of transition aluminas (mixture of κ-, δ-, and γ-phases) was observed at higher temperatures (>1200 °C). The ceramic−glass (crystalline−amorphous) nature of the system was established by high-resolution transmission electron microscopy studies, while the compositions of the phases were determined by spatially resolved energy dispersive spectra. The infrared and solid-state ^{27}Al MAS NMR data of the film material showed spectral patterns formed by an overlapping of the signals corresponding to $LnAlO_3$ and Al_2O_3 phases. The ellipsometric studies revealed the refractive indices to be 1.76 and 1.67 for the Pr−O−Al and Nd−O−Al systems, respectively. The film growth rates were found to be in the range 1.7−1.8 μm/h at 500 °C.

Introduction

Active luminescent dopants, for instance, lanthanide (Ln) ions or their oxide phases embedded in isotropic matrices are technologically important materials as solid-state laser materials, phosphors, and optical amplifiers, etc.[1−4] A homogeneous dispersion of Ln^{3+} ions in a host matrix (e.g., SiO_2) is difficult due to their clustering tendency. In a three-dimensional −Ln−O−Si(M)− network, the large lanthanide cations reside as network modifiers requiring six to eight nonbridging oxygen for charge compensation; however, in the case of fully connected networks such as silica glass, the absence of nonbridging oxygen atoms results in a poor solubility (incorporation) of rare earth ions.[5] As a result, the Ln^{3+} ions form interaction clusters resulting in shorter decay time and quenching of the luminescence quantum yield. Alumina addition was found to improve the dissolution of rare-earth ions in silica glasses prepared by vapor-phase deposition or melting.[6] The addition of alumina as a codopant effectively eliminates the microclustering by improving the ill-coordinated state of lanthanide centers in which Al_2O_3 forms a solvation shell of AlO_4 and/or AlO_6 units around the Ln^{3+} ions, thus keeping them homogeneously dispersed.[7,8] It was found that in the Ln_2O_3–SiO_2 glasses

* To whom correspondence should be addressed. E-mail: mathur@ch11sgi0.anchem.uni-sb.de.
[†] Institute of Inorganic Chemistry.
[‡] Institute of Experimental Physics.
[§] Institute of New Materials.

(1) Beecroft, L. L.; Ober, C. K. *Chem. Mater.* **1997**, *9*, 1302.
(2) Tissue, B. M. *Chem. Mater.* **1998**, *10*, 2837.
(3) Bender, C. M.; Burtlich, J. M.; Barber, D.; Pollock, C. *Chem. Mater.* **2000**, *12*, 1969.
(4) Blasse, G. *Chem. Mater.* **1989**, *1*, 294.
(5) Arai. K.; Namikawa, H.; Kumata, K.; Ishi, Y.; Tanaka, H.; Iida, I. *Jpn. J. Appl. Phys.* **1983**, *22*, L397.
(6) Fujiyama, T.; Yokoyama, T.; Hori, M.; Sasaki, M. *J. Non-Cryst. Solids* **1991**, *135*, 198.
(7) Ikesue, A.; Kinoshita, T.; Kamata, K.; Yoshida, K. *J. Am. Ceram. Soc.* **1995**, *78*, 1033.
(8) Patra, A.; Reisfeld, R.; Minti, H. *Mater. Lett.* **1998**, *37*, 325.

10.1021/cm011092+ CCC: $20.00
Published on Web 10/13/2001

codoped with Al_2O_3, the Ln^{3+} ions are preferentially surrounded by Al−O bonds.[9] The approaches commonly practiced to obtain Ln−O−Al ceramics are based on vaporization or melting of different precursors (e.g., oxides or halides) which suffer from the differential vapor pressures of the individual sources and the contamination of the films by halide ions deleterious for the film quality.[10,11] An alternative route to solid-state materials is the use of molecular compounds containing the component metals in chemical vapor deposition (CVD) or sol−gel processes to obtain high-purity films or powders. In the CVD processes, bimetallic oxides are generally deposited using multiple sources to achieve the desired composition.[12] In this context, we were interested in a single-stage synthesis of Ln−O−Al films using precursors containing *preformed* Ln−O−Al bonds. In a preliminary communication,[13] we have reported on the formation of a $NdAlO_3/Al_2O_3$ composite by chemical vapor deposition of the precursor $[NdAl_3(OPr^i)_{12}(Pr^i\text{-}OH)]$. We and others have reported on the potential advantages of using molecular precursors in the CVD process.[14−19]We describe here a complete study on the synthesis and characterization of $PrAlO_3/Al_2O_3$ and $NdAlO_3/Al_2O_3$ composites and the inherent advantages of using *single-source* molecules to obtain composites based on chemically controlled dispersion of one phase into the other.

Experimental Section

Chemicals. The syntheses of alkoxide precursors and other experimental manipulations were performed in a modified Schlenk type vacuum assembly, taking stringent precautions against atmospheric moisture. Solvents were purified by standard methods and stored over appropriate desiccating agents. The $PrCl_3$ and $NdCl_3$ (Aldrich) were dried in a vacuum (110 °C/10^{-2} Torr) and analyzed for chlorine contents before use. Praseodymium and neodymium amides, $[Ln\{N(SiMe_3)_2\}_3]$ (Ln(III) = Pr, Nd) were synthesized by the reaction of $LnCl_3$ with 3 equiv of lithium hexamethyl disilazide.[20] The Praseodymium and neodymium isopropoxides were in-situ generated from respective amides by their reactions with isopropyl alcohol. Aluminum isopropoxide was synthesized by the reaction of Al turnings with Pr^iOH in the presence of small amounts of $HgCl_2$ (catalyst).[21]

X-ray Crystallography. The single crystals of $[Pr\{Al(OPr^i)_4\}_3(Pr^iOH)]$ (**1**) and $[Nd\{Al(OPr^i)_4\}_3(Pr^iOH)]$ (**2**), suitable for X-ray diffraction, were grown from toluene−isopropyl alcohol mixtures, left to stand at room temperature (12 h). Compounds **1** and **2** crystallize in significant yields (70−75%) as green and purple colored blocks, respectively. Data were collected on a Siemens Stoe AED 2 diffractometer operating with graphite monochromated Mo Kα X-ray radiation (λ = 0.710 73 Å). Unit cell dimensions, determined from the least-squares refinement of $(\sin\theta/\lambda)^2$ values for 25 accurately centered reflections, showed **1** and **2** to be isotypical, which was further proven by the refinement of the structures. Crystal data and structural refinement parameters are given in Table 1. The intensities were corrected for Lorentz and polarization factors, and a semiempirical absorption correction (φ scans) was applied in both cases. The absence of any diffraction symmetry suggested the possible space group to be $P1$ or $P\bar{1}$. The structure was solved in both centrosymmetric ($P\bar{1}$) and accentric ($P1$) options. The space group $P\bar{1}$ was proved to be the correct choice by successful refinement of the model and by applying the statistical methods. The structure solution and refinement, in both cases, were performed using SHELXS-86 and SHELXS-97 programs.[22,23]

Table 1. Pertinent Crystallographic Data of Compounds 1 and 2

empirical formula	$C_{39}H_{92}Al_3O_{13}Pr$	$C_{39}H_{92}Al_3NdO_{13}$
MW	991.25	994.31
cryst syst	triclinic	triclinic
space group	$P\bar{1}$	$P\bar{1}$
a/Å	12.953(3)	12.932(3)
b/Å	13.772(3)	13.779(3)
c/Å	18.620(4)	18.580(4)
α/deg	75.41(3)	75.51(3)
β/deg	85.71(3)	85.76(3)
γ/deg	62.82(3)	62.82(3)
U/Å^3	2856.4(11)	2848.4(11)
Z	4	4
F(000)	1124	1058
D_c/(Mgcm^{-3})	1.192	1.159
T/°C	293(2)	293(2)
cryst size/mm	0.30 × 0.25 × 0.18	0.40 × 0.30 × 0.22
diffractometer	Stoe AED 2	Stoe AED 2
scan type	$\omega-\theta$	$\omega-\theta$
reflcns collcd	7453	7425
independ reflcns	7453	7425
obsd reflcns	6771	6698
GOF on F^2	0.948	1.052
final R indices (R1; $I > 2\sigma(I)$)	0.0425	0.0415
R indices (R1; all data)	0.0487	0.0493

Instrumentation. The C and H contents in the film material were obtained using a LECO CHN900 elemental analyzer. The infrared spectra were recorded on a BioRad FT-IR Spectrometer-165, after pelletizing the delaminated CVD deposits with KBr. Powder X-ray diffraction (XRD) measurements were performed on a STOE diffractometer operating with a Cu Kα radiation at room temperature. The scanning electron microscopy (SEM) and energy-dispersive X-ray (EDX) analysis were carried out in the specimen chamber of an EDX coupled scanning electron microscope CAM SCAN S4. The atomic force microscopic images were recorded using silicon or silicon nitride tips on a Nanoscope III of Digital Instruments. The transmission electron microscopy (TEM) images were recorded on a JEM 200 CX transmission electron microscope. High-resolution electron micrographs were obtained on a CM-200 FEG (Philips) transmission electron microscope equipped with a field emission gun operating at 200 kV. The ^{27}Al magic angle spinning (MAS) solid-state NMR spectra were recorded on a Bruker MSL-200 spectrometer using $AlCl_3$ as an external standard. The depth resolved elemental distribution, in the films, was obtained by glow discharge mass

(9) Thomas, I. M.; Payne, S. A.; Wilke. G. D. *J. Non-Cryst. Solids* **1992**, *151*, 183.
(10) Esparza, A.; Garcia, M.; Falcony, C. *Thin Solid Films* **1998**, *14*, 325.
(11) Arai, K.; Namikawa, H.; Kumata, K.; Honda, T.; Ishi, Y.; Handa, T. *J. Appl. Phys.* **1986**, *59* (10), 3430.
(12) Deschanvres, J. L.; Meffre, W.; Joubert, J. C.; Senateur, J. P.; Robaut, F.; Broquin, J. E.; Rimet, R. *J. Alloys Compd.* **1998**, *275*, 742.
(13) Veith, M.; Mathur, S.; Lecerf, N.; Bartz, K.; Heintz, M.; Huch, V. *Chem. Mater.* **2000**, *12*, 271.
(14) Special Issue on: Proceedings of the Twelfth European Conference on CVD. *J. Phys. IV* **1999**, *9*.
(15) Veith, M.; Mathur, S.; Lecerf, N.; Shen, H.; Huefner, S. *Chem. Mater.* **1999**, *11*, 3103.
(16) Veith, M.; Altherr, A.; Lecerf, N.; Mathur, S.; Valtchev, K.; Fritscher, E. *Nanostruct. Mater.* **1999**, *12*, 191.
(17) Jones, A. C. *Chem. Vap. Deposition* **1999**, *4*, 169.
(18) Crosbie, M. J.; Wright, P. J.; Davies, H. O.; Jones, A. C.; Leedham, T. J.; O'Brien, P.; Critchow, G. W. *Chem. Vap. Deposition* **1999**, *5*, 9.
(19) Belot, J. A.; Wang, A.; McNeely, R. J.; Liable-Sands, L.; Rheingold, A. L.; Matks, T. J. *Chem. Vap. Deposition* **1999**, *5*, 2.
(20) Lappert, M. F.; Power, P. P.; Sanger, A. R.; Srivastava, R. C. *Metal and Metalloid Amides*; Wiley: New York, 1980.
(21) Bradley, D. C.; Mehrotra, R. C.; Gaur, D. P. *Metal Alkoxides*; Academic Press: London, 1978.
(22) Sheldrick, G. M. *SHELXS-86, Program for Crystal Structure Determination*; University of Göttingen: Göttingen, Germany, 1986.
(23) Sheldrick, G. M. *SHELXL-97, Program for Crystal Structure Determination*; University of Göttingen: Göttingen, Germany, 1997.

spectrometry (GDMS) on a GLOQVAD spectrometer (VG Elemental) working with low-pressure argon discharge. The X-ray photoelectron spectroscopy (XPS) analyses were performed on a Surface Science Instrument (SSI) M-Probe using Al Kα radiation with a total instrumental resolution (fwhm = full width at half-maximum) of ca. 0.8 eV. The data were charge referenced to C 1s at a binding energy of −284.0 eV.

Results and Discussion

Synthesis and Characterization of Precursors. The synthesis of the mixed-metal alkoxides was based on the Lewis acid−base interactions of the constituent alkoxides using a slightly modified procedure.[24] The praseodymium or neodymium alkoxide was generated in-situ by the alcoholysis of the appropriate lanthanide tris-amido precursor and allowed to react with 3 equiv of aluminum isopropoxide (eq 1).[25] The reaction mixture was refluxed overnight, and the solvent was stripped in a vacuum to obtain green (**1**) and purple (**2**) colored solids, which crystallized as 2-propanol adducts from a hot mixture of isopropyl alcohol and toluene.

$$[\mathrm{Ln}\{\mathrm{N(SiMe_3)_2}\}_3] + 3[\mathrm{Al(O}Pr^i\mathrm{)_3}]_4 \xrightarrow{Pr^i\mathrm{OH/C_7H_8}} [\mathrm{Ln}\{\mathrm{Al(O}Pr^i\mathrm{)_4}\}_3(Pr^i\mathrm{OH})] \quad (1)$$

$$\mathrm{Ln} = \mathrm{Pr}\ (\mathbf{1});\ \mathrm{Nd}\ (\mathbf{2})$$

The lanthanide−aluminum alkoxides of the general formula $[\mathrm{Ln}\{\mathrm{Al(O}Pr^i\mathrm{)_4}\}_3]$ have been synthesized by Mehrotra and co-workers by salt elimination reactions between $LnCl_3$ and alkali-metal (M) alkoxo-aluminates, $[MAl(OR)_4]$.[26,27] However, the efforts of other workers on the isolation and structural characterization of these systems have reported on the preferential formation of oxo-alkoxide clusters of the general formula $M_5O(OR)_{13}$ or retention of halide and/or alkalimetal ions in the final products to form "ate" species.[28−31] To establish the identity of the heterometal alkoxides and to avoid the possibility of salt retention, we have modified the synthesis as shown in eq 1. Indeed, this "salt-free" approach yields pure Ln−Al complexes in high yields. To rule out the prevailing ambiguities regarding the heterometallic nature of Ln−Al systems, **1** and **2** were characterized by single-crystal X-ray diffraction analysis, which corroborates the synthetic observations and structural proposals of Mehrotra and co-workers.[24−26]

The solid-state structures of **1** and **2** are isotypical (Table 1). The unit cell in each of the cases contains two crystallographically independent molecules with slightly different bond parameters (Tables 2 and 3) but an overall similar structure. Since the crystals are centrosymmetric, both forms of enantiomers are present in the crystal. A pseudo-3-fold screw axis passes through the lanthanide elements. The molecular formulation is based on a central Ln^{3+} (Ln = Pr, Nd) cation whose charge is compensated by three monoanionic tetra-isopropoxo aluminate units ($\{\mathrm{Al(O}Pr^i\mathrm{)_4}\}^-$) (Figure 1). In both the cases, an additional alcohol molecule was found to be coordinated to the lanthanide center to provide a 7-fold coordination. The coordination geometry around Pr (Figure 1) can be described as halfway between a distorted trigonal prism and a monocapped octahedron; however, the distortion in bond angles supports the former case. A number of examples containing seven-coordinate lanthanide atom have been structurally characterized which reflect the tendency of Ln(III) ions to prefer a prismatic geometry over an octahedral ligand environment.[32,33] The coordination figures of Al atoms coordinated by four isopropoxy groups resemble a distorted tetrahedron. The short distance (2.819 Å) between O(6) and O(10) shows the presence of a hydrogen bridging between the two atoms (Figure 1). In fact, the hydrogen atom on the coordinated alcohol molecule could be located in the structure calculations. Among the Al−O distances, the Al-μ-(OPr^i) distances (1.724(4)−1.799(4) Å) are longer than the terminal ones

Table 2. Selected Bond Distances (Å) of Compound 1

molecule A		molecule B	
Pr(1)−O(1)	2.385(16)	Pr(2)−O(14)	2.390(15)
Pr(1)−O(2)	2.381(14)	Pr(2)−O(15)	2.407(14)
Pr(1)−O(3)	2.385(16)	Pr(2)−O(16)	2.442(13)
Pr(1)−O(4)	2.412(12)	Pr(2)−O(17)	2.472(11)
Pr(1)−O(5)	2.386(11)	Pr(2)−O(18)	2.517(11)
Pr(1)−O(6)	2.617(10)	Pr(2)−O(19)	2.456(15)
Pr(1)−O(7)	2.543(10)	Pr(2)−O(20)	2.525(15)
Al(2)−O(1)	1.820(16)	Al(5)−O(14)	1.781(18)
Al(1)−O(2)	1.796(16)	Al(4)−O(15)	1.790(15)
Al(3)−O(3)	1.777(17)	Al(6)−O(16)	1.773(15)
Al(2)−O(4)	1.771(12)	Al(5)−O(17)	1.809(13)
Al(1)−O(5)	1.782(15)	Al(4)−O(18)	1.821(14)
Al(3)−O(7)	1.755(13)	Al(6)−O(19)	1.806(16)
Al(2)−O(8)	1.750(15)	Al(5)−O(21)	1.660(14)
Al(1)−O(9)	1.754(14)	Al(6)−O(22)	1.708(16)
Al(3)−O(10)	1.748(17)	Al(4)−O(23)	1.603(16)
Al(2)−O(11)	1.722(17)	Al(5)−O(24)	1.684(15)
Al(3)−O(12)	1.592(18)	Al(6)−O(25)	1.679(14)
Al(1)−O(13)	1.664(16)	Al(4)−O(26)	1.721(15)

Table 3. Selected Bond Distances (Å) of Compound 2

molecule A		molecule B	
Nd(1)−O(1)	2.408(12)	Nd(2)−O(14)	2.387(16)
Nd(1)−O(2)	2.345(14)	Nd(2)−O(15)	2.413(14)
Nd(1)−O(3)	2.384(15)	Nd(2)−O(16)	2.408(14)
Nd(1)−O(4)	2.381(14)	Nd(2)−O(17)	2.466(12)
Nd(1)−O(5)	2.349(13)	Nd(2)−O(18)	2.500(13)
Nd(1)−O(6)	2.592(12)	Nd(2)−O(19)	2.444(16)
Nd(1)−O(7)	2.531(11)	Nd(2)−O(20)	2.524(15)
Al(2)−O(1)	1.824(15)	Al(5)−O(14)	1.763(18)
Al(1)−O(2)	1.796(17)	Al(4)−O(15)	1.791(16)
Al(3)−O(3)	1.745(17)	Al(6)−O(16)	1.814(17)
Al(2)−O(4)	1.789(15)	Al(5)−O(17)	1.794(14)
Al(1)−O(5)	1.807(16)	Al(4)−O(18)	1.801(15)
Al(3)−O(7)	1.786(14)	Al(6)−O(19)	1.756(18)
Al(2)−O(8)	1.695(18)	Al(5)−O(21)	1.687(15)
Al(1)−O(9)	1.698(16)	Al(6)−O(22)	1.736(16)
Al(3)−O(10)	1.705(19)	Al(4)−O(23)	1.658(18)
Al(2)−O(11)	1.726(18)	Al(5)−O(24)	1.685(16)
Al(3)−O(12)	1.569(18)	Al(6)−O(25)	1.701(14)
Al(1)−O(13)	1.649(17)	Al(4)−O(26)	1.721(15)

(24) Meyer, F.; Hempelmann, R.; Mathur, S.; Veith, M. *J. Mater. Chem.* **1999**, *9*, 1755.
(25) Veith, M.; Mathur, S.; Kareiva, A.; Jillavi, M.; Zimmer, M.; Huch, V. *J. Mater. Chem.* **1999**, *9*, 3069.
(26) Mehrotra, R. C.; Aggarwal, M. M.; Mehrotra, A. *Synth. React. Inorg. Met-Org. Chem.* **1973**, *3*, 181.
(27) Mehrotra, R. C.; Mehrotra, A. *Indian J. Chem., Sect A* **1972**, *10*, 532.
(28) Poncelet, O.; Sartain, W. J.; Hubert-Pfalzgraf, L. G.; Folting, K.; Caulton, K. G. *Inorg. Chem.* **1989**, *28*, 263.
(29) Bradley, D. C.; Chudzynska, H.; Frigo, D. M.; Hammond, M. E.; Hursthouse, M. B.; Mazid, M. A. *Polyhedron* **1990**, *9*, 719.
(30) Andersen, R. A.; Templeton, D. H.; Zalkin, A. *Inorg. Chem.* **1978**, *17*, 1962.
(31) Evans, W. J.; Sollberger, M. S. *Inorg. Chem.* **1988**, *27*, 4417.
(32) Mehrotra, R. C.; Singh, A.; Tripathi, U. M. *Chem. Rev.* **1991**, *91*, 1287.
(33) Tripathi, U. M.; Singh, A.; Mehrotra, R. C.; Goel, S. C.; Chiang, M. Y.; Buhro, W. E. *J. Chem. Soc., Chem. Commun.* **1992**, 152.

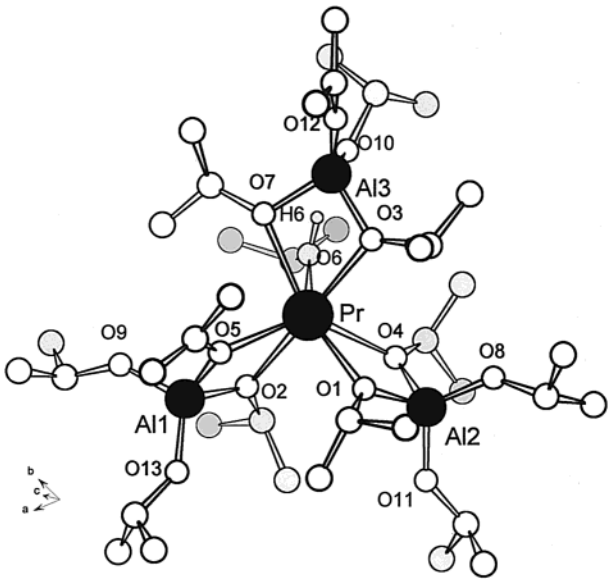

Figure 1. Molecular structure of [Pr{Al(O*Pr*^{i})$_4$}$_3$(*Pr*^{i}OH)] (**1**).

(Al−O*Pr*^{i}, 1.655(5)−1.731(5) Å). The bond length dispersions in the Pr and Nd coordination polyhedra are small, indicating a strong binding of the three bidentate {Al(O*Pr*^{i})$_4$}$^-$ anions to the Ln^{3+} centers, which imparts the observed stability to Pr−O−Al and Nd−O−Al bridges, in the gas phase.

Although **1** and **2** crystallize as alcohol adducts, the alcohol-free Ln−Al heterobimetallic alkoxides are also stable products and could be isolated by prolonged pumping of crystalline samples of **1** and **2** in vacuo (100 °C/10^{-2} Torr). Further, the compounds [Ln{Al(O*Pr*^{i})$_4$}$_3$] (Ln = Pr, Nd) could be distilled (120−125 °C/10^{-2} Torr) in vacuo as colored viscous products without any signs of decomposition. The elemental analyses of the distillates agrees with the formulation, LnAl$_3$(O*Pr*^{i})$_{12}$. In view of the similarities in the stereochemical behavior of lanthanide atoms, the PrAl$_3$(O*Pr*^{i})$_{12}$ and NdAl$_3$(O*Pr*^{i})$_{12}$ compounds are expected to possess the formula [LnAl$_3$(μ-O*Pr*^{i})$_6$(O*Pr*^{i})$_6$] (Ln = Pr, Nd). Mehrotra in his seminal work on heterometal alkoxides has proposed a structural model for [Ln{Al(O*Pr*^{i})$_4$}$_3$] (Ln = any trivalent lanthanide ion) derivatives in which a six-coordinate lanthanide atom is coordinated by three {Al(O*Pr*^{i})$_4$}$^-$ units. The structural characterization of **1** and **2** verifies the proposal of Mehrotra.[26,27]

Deposition and Characterization of Films. The gas-phase thermolysis of lanthanide isopropoxoaluminates [M{Al(O*Pr*^{i})$_4$}$_3$(*Pr*^{i}OH)] (M(III) = Pr (**1**), Nd (**2**)) has been studied in a CVD reactor with a cold-wall configuration. Compounds **1** and **2** were transported to the vapor phase by maintaining the reservoir at 95 °C. The precursor flux was guided to the hot substrate by applying vaccum (10^{-3} Torr) where a thermal reaction and deposition occurs. The volatile byproducts formed in the thermolysis were exhausted out in a mass spectrometer coupled to the deposition tube. The substrates were heated either by inductive means or by placing them upon a conducting target. During the CVD process, the substrate temperature was regulated by an infrared pyrometer. The complete experimental setup is described elsewhere.[34] The film growth was examined on both metallic (copper, steel) and nonmetallic (silicon, quartz) substrates, with the substrate temperature in the range of 450−550 °C. The process window between 450 and 550 °C revealed that significant deposition rates were obtained at 500 °C. The amount of carbon contents in the as-deposited oxide films was affected by the precursor flow, which was monitored by maintaining the precursor reservoir at different temperatures. The low carbon levels, in the deposits, obtained on decreasing the precursor flux suggest the surface adsorption is responsible for the film growth. The carbon concentration in the films is due to the entrapment of organic rests and incompletely decomposed precursor molecules. In fact, a controlled precursor flux reduces the level of pyrolytic carbon in the gas phase and ultimately in the films. The coatings were transparent green and purple for precursors **1** and **2,** respectively, and were found to be dense, uniform, and adherent in both the cases.

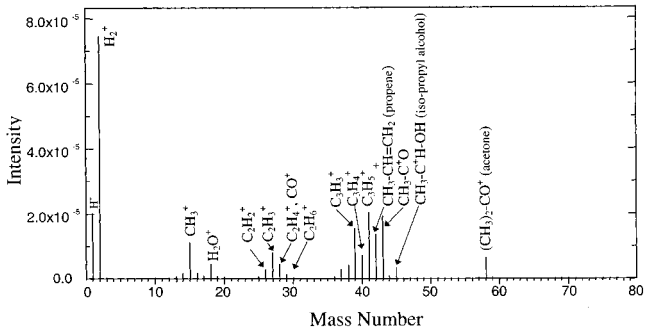

Figure 2. Typical mass spectral pattern observed during the chemical vapor deposition of **1** and **2** at 500 °C.

Decomposition Mechanism. For monitoring the decomposition process on-line, one of the outlets of the CVD reactor was connected to the mass spectrometer by a stainless steel tube fitted with a variable leak valve. The mass spectra recorded during the CVD of **1** and **2** reveal molecular peaks of light species and ionic fragments suggesting different mechanisms to be operative; however, it is difficult to say which mechanism (radical or ionic) predominates. Nevertheless, it is possible to identify the molecular peaks of the most abundant species. From the fragmentation patterns, the main byproducts were distinguished to be acetone, isopropyl alcohol, propene, and hydrogen with diagnostic peaks at m/z = 58, 45, 42, and 2, respectively. For an authentic identification of the gaseous products, the mass spectra of isopropyl alcohol, acetone, and propene were recorded under similar experimental conditions and sequentially stripped from the complete mass spectrum recorded during the CVD process (Figure 2). The only peaks remaining after subtracting the mass spectral features of (CH$_3$)$_2$CHOH, (CH$_3$)$_2$C=O, and H$_2$C=CH−CH$_3$ are characteristic of dihydrogen mass spectrum (m/z = 1 and 2), which support the decomposition pathway outlined in eq 2.

$$[\mathrm{Ln}\{\mathrm{Al}(\mathrm{O}Pr^i)_4\}_3(\mathrm{HO}Pr^i)] \xrightarrow{\text{CVD,500 °C}} \text{“}\mathrm{LnAl_3O_6}\text{”} + (x+1)Pr^i\mathrm{OH} + y\mathrm{CH_2{=}CH{-}CH_3} + z(\mathrm{CH_3})_2\mathrm{C{=}O} + m\mathrm{H_2} \quad (2)$$

(where $x/y \neq 1$; $x \gg y, z, m$; and $x + y + z = 12$).

The formation of the above products during the thermal decomposition of **1** and **2** was also confirmed

(34) Veith, M.; Kneip, S. *J. Mater. Sci. Lett.* **1994**, *13*, 335.

Scheme 1

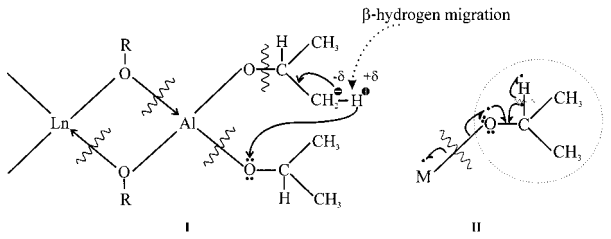

by condensation of the liberated gaseous products in a cold trap and then by recording of the NMR spectra. Most of the other peaks observed in Figure 2 correspond to the fragments of the above-mentioned products. For example, $m/z = 39$ (C_3H_3), presumably a dissociation product of propene, is a classic fragment of unsaturated straight chain hydrocarbons. The thermolysis of a metal−alkoxide bond in the case of isopropoxide or *tert*-butoxide derivatives probably initiates via a M−O bond cleavage or β-hydride migration/elimination (**I**, Scheme 1). The transfer of a β-hydrogen atom results in the formation of the parent alcohol and subsequent elimination of an alkene molecule (**I**). In the case of a C−O bond heterolysis, the formed Me_2CH^+ carbonium ion could also form H^+ and propene or can interact with isopropyl alcohol to give $Pr^i{}_2O$ and H^+; however, in the case of a homolytic metal−oxygen bond scission (**II**) the alkoxo radical may rearrange to form acetone, thereby eliminating a hydrogen radical. The isopropyl alcohol formed can undergo dehydration and/or dehydrogenation resulting in the formation of propene and acetone, respectively. These reactions are known to be catalyzed by metal oxide surfaces under vacuum.[35] Alternatively, the anionic fragment left after the hydride migration can rearrange itself with a simultaneous scission (cooperative mechanism) of the M−O bond to form acetone. The propene decomposition is apparently governed with a strong tendency to limit the number of hydrogen atoms in the hydrocarbon molecule. This observation is supported by a high-intensity peak for dihydrogen and the observation of molecular peaks for methane, ethyne, and ethylene at $m/z = 16$, 26, and 28, respectively.

Chemical Composition and Elemental Distribution. The determination of Nd and Al contents by chemical analysis of the solid deposits was in agreement (±1.0%) with the cation ratio present in the starting compounds. The energy dispersive X-ray (EDX) data of the films correspond to the lanthanide to aluminum ratios, in the molecular precursors (Ln:Al = 1:3), suggesting an intact transport of the molecular precursors in the gas phase. In addition, no metal segregation or heterogeneity was observed in the films on a submicrometer level, ruling out the possible dissociation of **1** and **2** into homometallic components. The quantification of the results, achieved by measuring standards and employing the SEM Quant software with a ZAF correction procedure, confirmed the formal composition to be $LnAl_3O_6$. Subject to the precursor flux, the carbon contamination in the films varied from 2 to 4.5 at. % as determined by the C and H analysis of the delaminated films. However, the carbon content was found to be significantly low (<0.3%) in the postannealed (800 °C) films. The X-ray photoelectron spectroscopy showed the carbon present in the films to be of graphitic nature (average binding energy, −284.4 eV); the carbidic carbon is observed at −282.4 eV.[36]

Phase Formation and Identification. The oxide films formed in the CVD could be delaminated by quenching hot substrates with a cold helium stream. The thermal shock caused by sudden cooling splits the film to give flakes of pure deposits that were grained and filled in glass capillaries for X-ray diffraction studies. The powder X-ray diffraction data of the as-deposited film (500 °C) shows broad peaks in the lower 2θ (23.70°) region indicative of incipient crystallization and short-range ordering present in the films. The equilibrium distance was calculated (Bragg equation) to be ca. 8 Å. The crystallization was observed on annealing the CVD films at 800 °C and the delaminated deposits at higher temperatures. The phase evolution in the heat-treated film material is evident in the powder XRD patterns of the solid formed during the CVD of **1** (Figure 3). The only crystalline component observed in the range 900−1200 °C was found to be $PrAlO_3$ (PDF File [29-076]).[37] Similarly, the XRD profiles of Nd−O−Al system show, until 1200 °C, Bragg peaks corresponding to rhombohedral $NdAlO_3$ (PDF File ([39-487]). The broadening of diffraction peaks indicates a rather small crystallite size as shown in the TEM images (see later). The particle size ($\langle d \rangle$) determined by Scherer formula[38] shows the average grain size to be 11, 18, and 28 nm at 900, 1000, and 1200 °C, respectively. The formal chemical composition (Ln:Al:O = 1:3:6, Ln = Pr, Nd) of the film and the identification of only the $LnAlO_3$ phase in the XRD measurements suggested the residual component(s) to be an amorphous aluminum oxide phase. This obvious implication was intriguing, especially in view of the tendency of alumina to crystallize at low temperatures (ca. 700−800 °C).[39] The presumption of amorphous alumina being the second component until 1200 °C was supported by the XRD analysis of the higher heat-treated powder, which revealed the crystallization of transition aluminas (mixture of κ[10-425], δ [04-877], and γ [04-878] phases) in the CVD deposits calcined at 1400 °C. The delayed crystallization of alumina and the steady growth of $LnAlO_3$ grains is an influence of the differential thermal properties of the individual phases. It should be noted that $NdAlO_3$ due to its excellent thermal conductivity is a favorable substrate for the Y−Ba−Cu−O superconducting oxides.[40] The preferential crystallization of $NdAlO_3$ can be attributed to the higher heat capacity of $NdAlO_3$ when compared with Al_2O_3 (Figure 4). It is known that a material with high heat capacity is heated more slowly than any material with low heat capacity when both are placed in a hot surrounding like an oven. As a result, the high heat capacity material can store more heat energy within its atomic structure at a given temperature. Therefore, the precondition for transition

(35) El-Nabarawy, Th.; Attia, A. A.; Alaya, M. N. *Mater. Lett.* **1995**, *24*, 319.

(36) *ESCA Handbook of X-ray Photoelectron Spectroscopy*; Perkin-Elmer: Eden Prairie, MN, 1992.

(37) Powder Diffraction Files, Card Nos. [29-076] and [39-487], 1990.

(38) Scherrer, P. *Göttinger Nachrichten* **1918**, *2*, 98.

(39) Veith, M.; Faber, S.; Hempelman, R.; Janssen, S.; Prewo, J.; Eckerlebe, H. *J. Mater. Sci.* **1996**, *31*, 2009.

(40) Morelli, D. T. *J. Mater. Res.* **1992**, *7*, 2492.

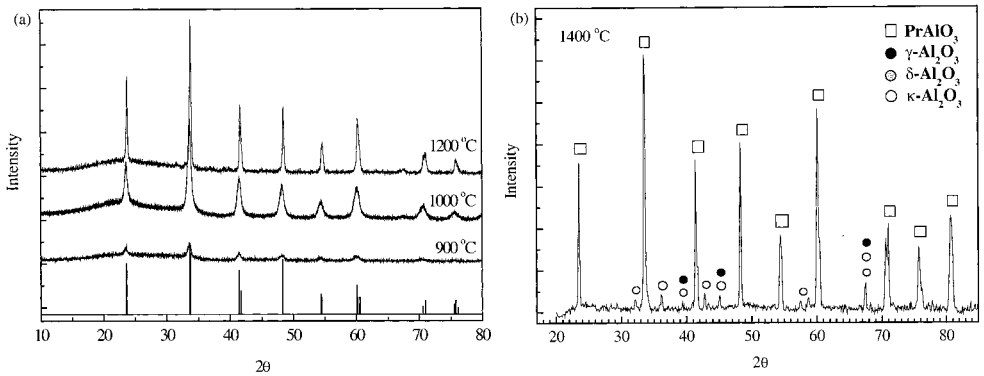

Figure 3. (a) Room-temperature XRD traces of the film material annealed at 900, 1000, and 1200 °C. (b) The CVD deposit heat treated at 1400 °C, showing the crystallization of aluminas (mixture of κ, δ, and γ phases) besides the $PrAlO_3$ phase.

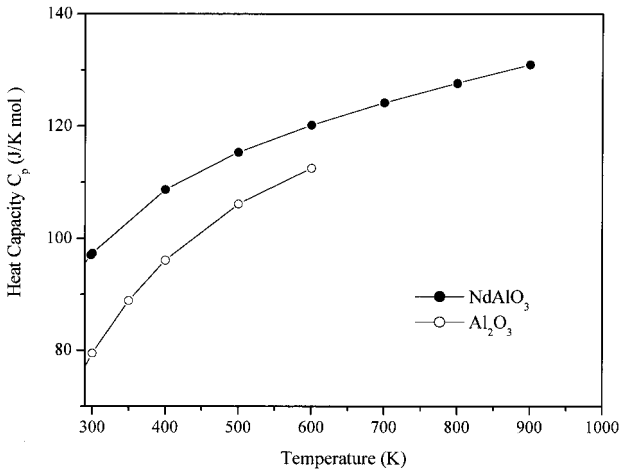

Figure 4. Temperature dependence of the heat capacity of $NdAlO_3$ and Al_2O_3 (data for the plot taken from refs 41 and 42, respectively).

from an isotropic to crystalline state is readily achieved due to high heat energy storage meeting the energy demand required for lattice diffusion. As a result, the crystallization of $NdAlO_3$ occurs first which on further heat treatment grows in an amorphous alumina (a-Al_2O_3) matrix. It was found that no experimental data for the thermal properties of nanocrystalline $NdAlO_3$ are available in the literature. In view of the above, the heat capacities of polycrystalline $NdAlO_3$[41] and Al_2O_3[42] were used for comparison sake (Figure 4). It is evident that the $NdAlO_3$ material has a higher heat capacity, and, thus, at a particular temperature the $NdAlO_3$ crystallites behave, on a heat energy scale, as hot zones (within the composite system), resulting in the preferential crystallization of the neodymium aluminate phase. The selective formation of $LnAlO_3$:Al_2O_3 composite in the annealed samples is probably due to the Ln−O−Al bonds existent in the amorphous $LnAl_3O_6$ material and the thermodynamic properties of the individual phases.

Film Morphology. The scanning electron micrograph of a Pr−O−Al film on silicon reveals an even surface (Figure 5a) made up of homogeneous spherical particles where each particle is constituted of several tiny crystallites. The cross-sectional views of an as-deposited and annealed (800 °C, 4 h) Nd−O−Al film are shown in Figure 5b,c, respectively. The results show the as-deposited film to be devoid of any structural features, which is typical for an amorphous growth. On the contrary, the annealing process induces crystallization, as evident in the nucleation of spherical grains across the film (Figure 5c). The AFM image (Figure 6) of a $PrAl_3O_6$ film recorded in contact mode supports the morphological features observed in the SEM studies. The 3D representation exhibits an even topology with an elevation (roughness) ranging from 20 to 30 nm. The small roughness and transparent nature of these films suggest the possibility of their use in integrated opto-electronic technology.

Crystallization and Particle Size Distribution. The transmission electron microscopy showed the as-obtained CVD deposits to be amorphous supporting the XRD observations. Upon postannealing, tiny crystals appeared in the amorphous matrix at 800 °C (Figure 7a), which were shown to be nanocrystallites of $PrAlO_3$ by spatially resolved EDX analysis performed randomly on different grains. The average crystallite size (10 nm) observed for the $PrAlO_3$ particles (dark grains in Figure 7a) is in agreement with the volume-weighted particle diameter (11 nm) obtained from the peak broadening of the X-ray diffraction profiles of a sample heat treated at 900 °C. The increase in grain size of the $PrAlO_3$ crystallites upon annealing at 1000 °C is corroborated by the TEM (Figure 7b) image, which exhibits crystallites of ca. 18 nm. The $PrAlO_3$ nanocrystals remain regularly dispersed in the amorphous Al_2O_3 phase, which makes the postannealed film material a ceramic−glass type composite, where a nanocrystalline component (ceramic) is embedded in an amorphous (glass) matrix. The high-resolution TEM image (Figure 8) shows crystalline domains dispersed in an amorphous matrix. It is noteworthy that alumina-based planar waveguide amplifiers show a significant enhancement in the net optical gain if the optically active element is homogeneously distributed throughout the waveguide.[43] Moreover, alumina is chosen as host material for the lanthanide elements because its crystal structure enables the incorporation of a high concentration of the dopant phase, leading to efficient pumping and amplification.[43,44] In view of the above, the $LnAlO_3/Al_2O_3$ nanocomposites are expected to show interesting optical

(41) van der Laan, R. R.; Konings, R. J. M.; van Genderen, A. C. G.; van Mittenburg, J. C. *Thermochim. Acta* **1999**, *1*, 329.
(42) Lide, D. R. *CRC Handbook of Chemistry and Physics*, 78th ed.; CRC Press: Boca Raton, FL, 1997−8.
(43) van den Hoven, G. N.; Koper, R. J. I. M.; Polman, A.; van Dam, C.; van Uffelen, J. W. M.; Smit, M. K. *Appl. Phys. Lett.* **1996**, *68* (1), 1886.
(44) van den Hoven, G. N.; van der Elsken, J. A.; Polman, A.; van Dam, C.; van Uffelen, K. W. M.; Smit, M. K. *Appl. Opt.* **1997**, *36*, 3338.

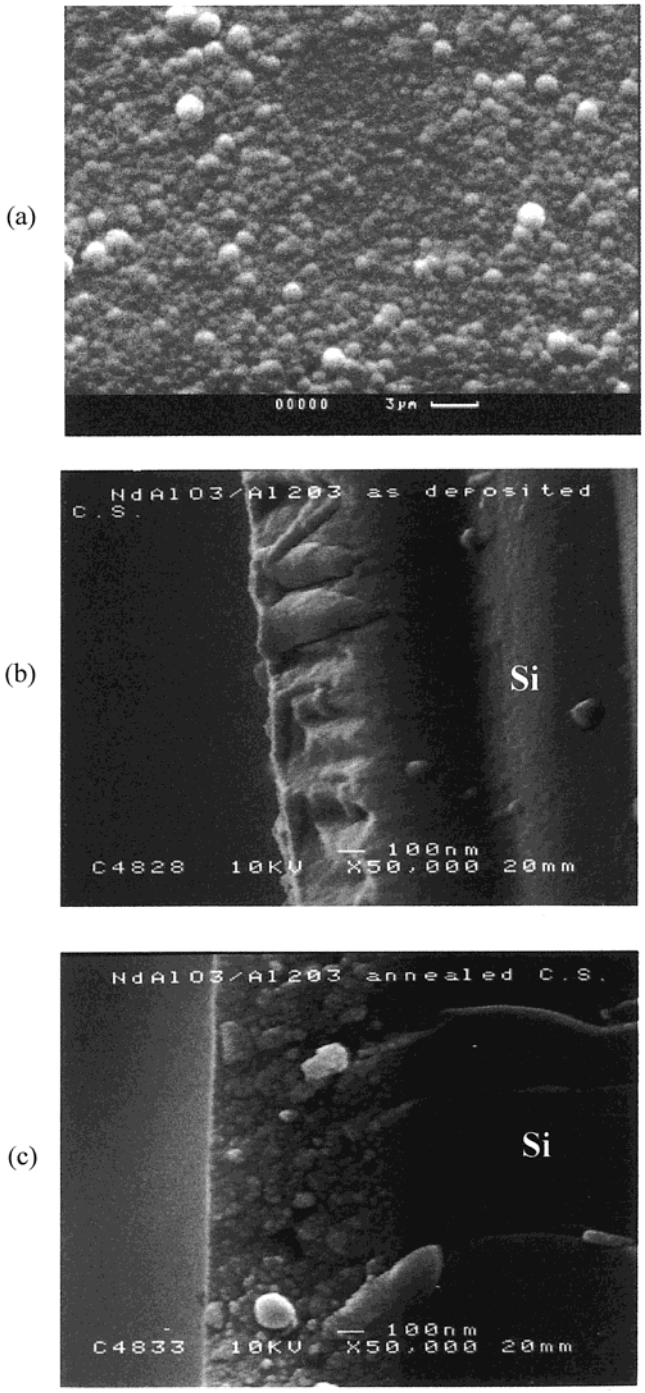

Figure 5. (a) Scanning electron micrographs of an as-deposited Pr−O−Al CVD film at ×3000 magnification (reproduced at 85% of original size). (b, c) SEM cross-section images of an as-deposited and annealed Nd−O−Al CVD film.

properties. Additionally, the TEM micrographs show that the $LnAlO_3$ nanocrystals wrapped by many tiny Al_2O_3 particles are shielded from each other, which should reduce, in principle, the concentration quenching effects. For evaluating the matrix effect, we have measured the photoluminescence of nanocrystalline samples of monophasic $NdAlO_3$ and $NdAlO_3/Al_2O_3$ composites, which verifies our hypothesis.[45]

Depth Profile. The glow discharge mass spectrometric (GDMS) profiles, obtained by gradually eroding away the surface by an incident argon ion beam probe, represent the depth-resolved quantitative composition and the consistency level of the lanthanide to aluminum ratio in the film bulk. The depth profile obtained for as-deposited Pr−O−Al system (Figure 9) shows the data after applying RSF (relative sensitivity factor) correction, the variation in abundance/concentration of different elements. The RSF values provide a measure of the emission intensity of a specific element essential for a quantitative analysis.[46] To determine the RSF factors, a stoichiometric mixture of pure aluminum and praseodymium (or neodymium) oxides in molar ratio 3:1 was pelletized with silver powder functioning as a conductive matrix to avoid charging problems.[46] Using the known RSF values for oxidic systems (O = 6.8; Al = 0.621; Fe = 0.59), the RSF for Pr was calculated (0.3) and employed to quantify the elemental ratios. The GDMS profile of a Pr−O−Al film shows three distinct regions: (i) the first part represents an adsorbate film formed by atmospheric contaminants (CO_2 and H_2O) as indicated by the increased level of signals due to carbon and oxygen in the scan range 0−5; (ii) the second and the most significant part spans scan numbers from 5 to 40 and reveals the consistency of element ratios across the film; (iii) the region at scan numbers above 40 shows a steady decrease in the signals corresponding to the elements present in the film and a simultaneous dominance of the signal due to the substrate material (Fe). The molar ratio for Pr, Al, and O obtained by plotting the element ratios against the number of scans shows the Pr:Al and O:Al ratios to be 1:3 and 2:l, respectively, which corresponds to the film composition determined by chemical, EDX and ESCA analyses.

Phase Evolution. The infrared spectrum of an annealed (800 °C) Nd−O−Al film shows absorptions due to the metal−oxygen vibrations in the range 900−440 cm^{-1} (Figure 10). To identify the Nd−O, Al−O, and Nd−O−Al frequencies, the observed IR spectrum was deconvoluted (curve a, Figure 10) assuming a Gaussian shape for the individual components. In addition, we have recorded the infrared spectra of nanocrystalline samples of $NdAlO_3$ and Al_2O_3 ceramics (curves b and c). Component 1 (curve a) represents a weak intensity broad band observed in the range 1400−1600 cm^{-1} probably due to HCO_3^- or H_2O adsorbed on the film surface.[47] The adsorption of these contaminants, as observed in the depth profiles of the films, is generally observed when films are allowed to stand under ambient conditions for longer time. Component 2 is a broad band centered at 874 cm^{-1} and corresponds to the absorption band of AlO_6 octahedrons.[48] Component 3 gives rise to the shoulder at 687 cm^{-1} and is dominated by the stretching in AlO_6 octahedrons.[48,49] The Al−O−Al stretching frequencies for tetrahedral Al are also observed in this region. The sharp peak at 440 cm^{-1} is assignable to the Nd−O stretching vibrations, whereas the Nd−O−Al frequencies are presumably observed around ca. 700 cm^{-1} (cf. curve b). The small intensity around 1070

(45) Mathur, S.; Veith, M.; Shen, H.; Hüfner, S.; Jillavi, M. *Chem. Mater.*, accepted.

(46) Harrison, W. W.; Hess, K. R.; Marcus, R. K.; King, F. L. *Anal. Chem.* **1986**, *58* (2), 3411.

(47) Lecerf, Nicolas Ph.D. Thesis, Saarland University, Saarbruecken, Germany, 1999.

(48) Saraswati, V.; Rao, G. V. N.; Rao, G. V. Rama *J. Mater. Sci.* **1987**, *22*, 2529.

(49) Adak, A. K.; Pathak, A.; Pramanik, P. *J. Mater. Sci. Lett.* **1999**, *17*, 559.

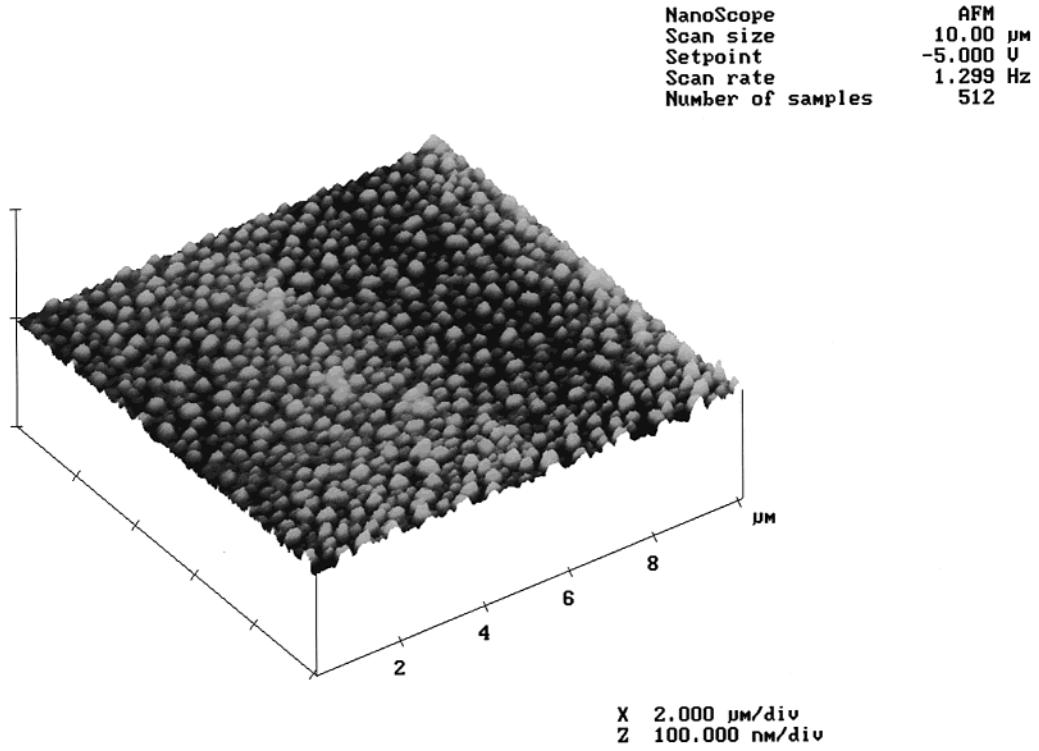

Figure 6. 3D representation of an AFM image of a Pr−O−Al film deposited at 500 °C on a silicon wafer.

cm^{-1} is characteristic of Al−OH bending vibrations.[50] The IR spectroscopic signatures of amorphous materials are generally difficult to distinguish or deconvolute, and the structural differences among the various alumina phases makes a detailed interpretation of the IR data rather difficult. Nevertheless, the summation of the IR spectra of $NdAlO_3$ and Al_2O_3 samples corresponds to the IR spectrum observed for the Nd−O−Al film, which suggests that although amorphous (XRD), the local structure of the as-deposited film is close to $LnAlO_3$:Al_2O_3 composite.

The solid-state ^{27}Al NMR data are complementary to the phase characterization and provide evidence about the Al distribution particularly in cases where powder X-ray diffration cannot provide conclusive information due to lack of long-range ordering as observed in the present case. The ^{27}Al NMR chemical shifts are characteristic of the local coordination at the Al nucleus and the different Al(III) sites, e.g., octahedral AlO_6, (0−30 ppm),[51] trigonal bipyramidal or square pyramidal AlO_5 (30−50 ppm),[52] and tetrahedral AlO_4 (50−100 ppm),[53] thus making the ^{27}Al magic angle spinning (MAS) NMR spectroscopy a diagnostic probe for investigating phase transformations in Al containing materials.[31,54,55] Since the film composition was established to be $LnAl_3O_6$ (Ln = Nd, Pr), by several analytical techniques (EDX, ESCA, GDMS), the identification of the amorphous component was of obvious interest. The only phase observed in the XRD patterns of ceramics sintered until 1200 °C corresponds to $PrAlO_3$ (PDF: [29-076]) or $NdAlO_3$ (PDF: [39-487]. The Figure 11 shows the ^{27}Al MAS NMR spectra of the as-obtained coating deposited at 500 °C and after heat treatment at 1000 °C. Before annealing, the product shows only one resonance at 7 ppm characteristic of 6-fold coordinated Al(III) center (Figure 11a); however, the different intensities of the first-order sidebands indicate another Al-containing component with a low coordination around aluminum. On the other hand, the sample sintered at 1000 °C shows two distinct resonances corresponding to the presence of two chemically different Al(III) species. The central transition band at 8 ppm is diagnostic of octahedrally coordinated aluminum; the high crystallinity of this phase is evident in the well-formed sidebands.[51] The second resonance at 60 ppm with first-order sidebands at 140 ppm falls within the range associated with Al in tetrahedral coordination. The satellite sidebands show no splitting corresponding to AlO_6 and AlO_4 sites (inset, Figure 11b) which would be the case for well-developed alumina phases. The non-observance of the sidebands due to tetrahedrally coordinated Al species is consistent with the presence of an amorphous Al_2O_3 phase as indicated by XRD data.

X-ray Photoemission Spectra. X-ray photoelectron spectroscopy (XPS) was used to monitor the elemental composition and the oxidation states of the lanthanide and aluminum atoms located on the surface of the films. The samples were analyzed at 35° take off angle corresponding to an analyzed depth of ca. 4−5 nm. Figure 12 shows the Al 2p peaks of the Pr−O−Al system. For comparison sake, the XPS data was also obtained for an Al_2O_3 film prepared by CVD of $[Al(OPr^i)_3]_4$ under conditions identical to those used in the CVD of **1** and **2**. In comparison to Al_2O_3, the peak shape for Al 2p peak in Pr−O−Al film shows asymmetry on

(50) Chane-Ching, J.-Y.; Klein, L. C. *J. Am. Ceram. Soc.* **1988**, *71*, 86.
(51) Veith M.; Altherr, A.; Wolfanger, H. *Adv. Mater., CVD* **1999**, *5*, 87.
(52) Muller, D.; Gessner, W.; Behrens, H. J.; Scheller, G. *Chem. Phys. Lett.* **1981**, *79* 59.
(53) Alemany, L. B.; Kerker, G. W. *J. Am. Chem. Soc.* **1986**, *108*, 6158.
(54) Hallas, E.; Sternberg, U. *Mol. Phys.* **1989**, *68*, 315.
(55) Bonhomme-Coury, L.; Babonneau, F.; Livage, J. *Chem. Mater.* **1993**, *5*, 323.

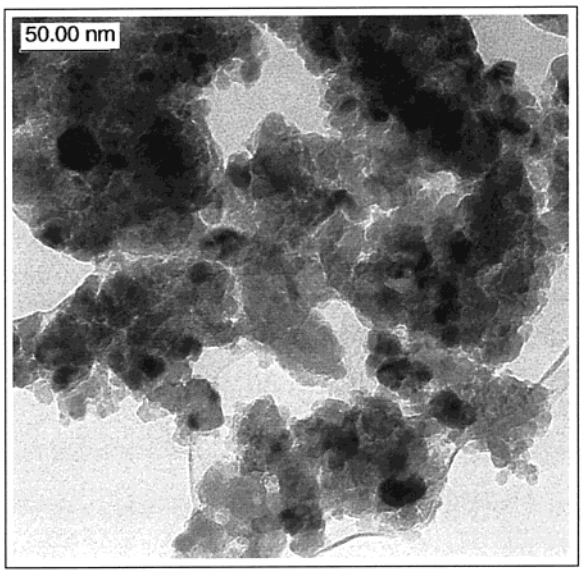

(a)

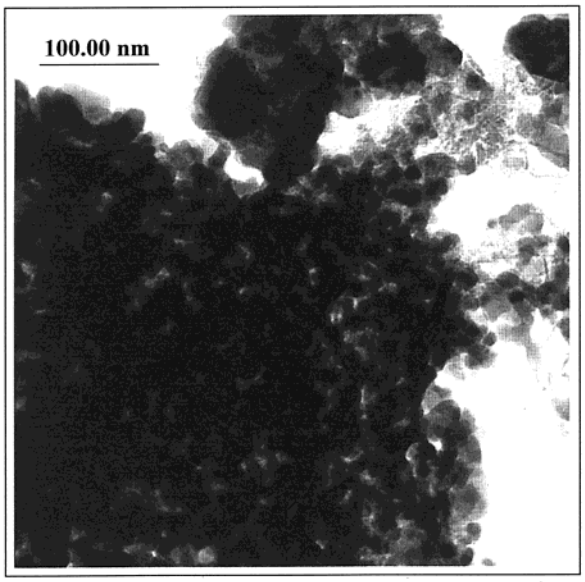

(b)

Figure 7. TEM images of the delaminated deposit after heat treatment at 800 (a) and 1000 °C (b), respectively.

the low-E_b side. Indeed, the Al 2p peak could be deconvoluted to two components (Figure 12, A and B). The Al 2p peak in pure Al_2O_3 is found at −75.4 eV. In view of the above, the two components (−75.2 and −74.0 eV) present in 2:1 ratio in the Pr−O−Al film can be attributed to the aluminum ions located in different chemical surrounding, namely, $PrAlO_3$ and Al_2O_3. A similar two-component Al 2p peak was also observed for the Nd−O−Al film. This finding is also supported by the ^{27}Al NMR results (Figure 11). Figure 13 shows the 3d XPS spectra of Pr−O−Al and Nd−O−Al films. It is known that, in an abundance of oxygen, the Pr ion tends to change its oxidation state from +3 in Pr_2O_3 to +4 in PrO_2. For intermediate oxygen concentrations, PrO_x sites ($1.5 < x < 2$) with different coordination numbers can exist which allow for a stable trivalent and/or tetravalent Pr state.[36,56] To determine unambiguously the oxidation state of Pr in the films, the Pr 3d peak

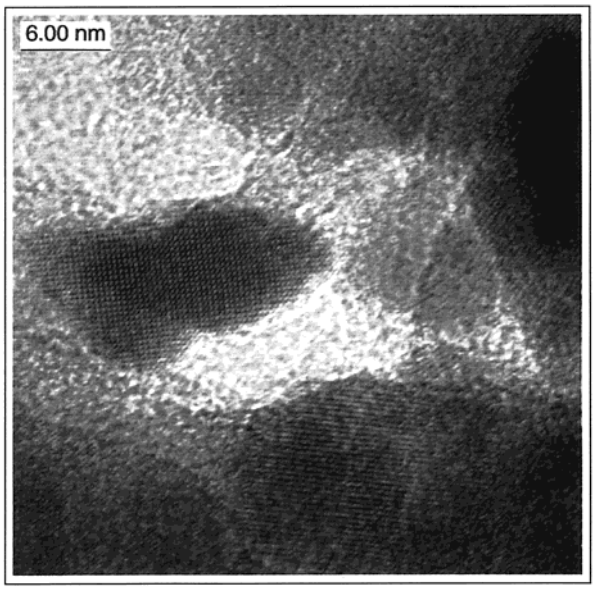

Figure 8. HR-TEM image showing the lattice fringes of the $PrAlO_3$ phase in the $PrAlO_3/Al_2O_3$ composite. The amorphous grains are Al_2O_3 particles.

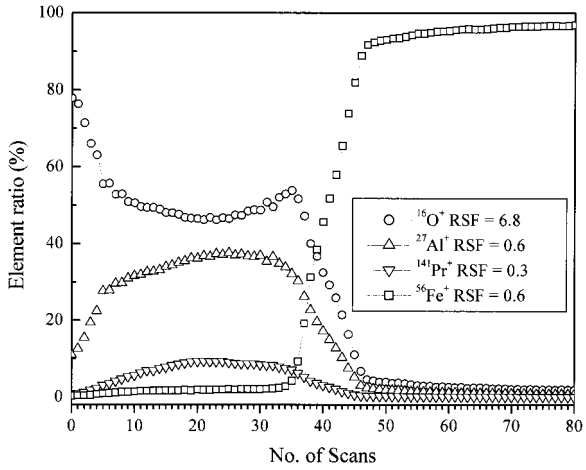

Figure 9. GDMS depth profile of a Pr−O−Al film deposited on steel, after applying the RSF correction.

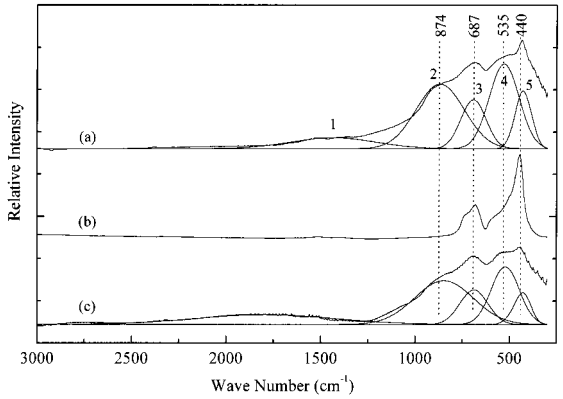

Figure 10. FT-IR spectra of (a) as-deposited Nd−O−Al film, (b) $NdAlO_3$, and (c) Al_2O_3.

was compared with that of a Pr_6O_{11} standard. The peak located at −980 eV in the XPS spectrum (Figure 13a) of the Pr−O−Al film can be attributed to oxygen 1s

(56) Kashii, N.; Maekawa, H.; Hinatsu, Y. *J. Am. Ceram. Soc.* **1999**, *82*, 1844.

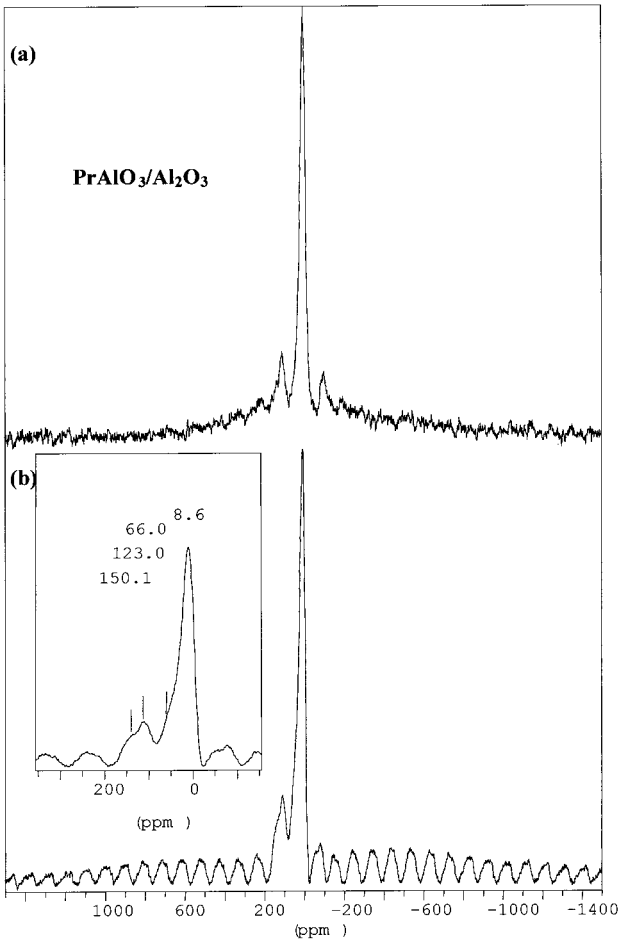

Figure 11. ^{27}Al solid-state MAS NMR spectra of (a) as-deposited Pr−O−Al film material and (b) after heat treatment at 1000 °C.

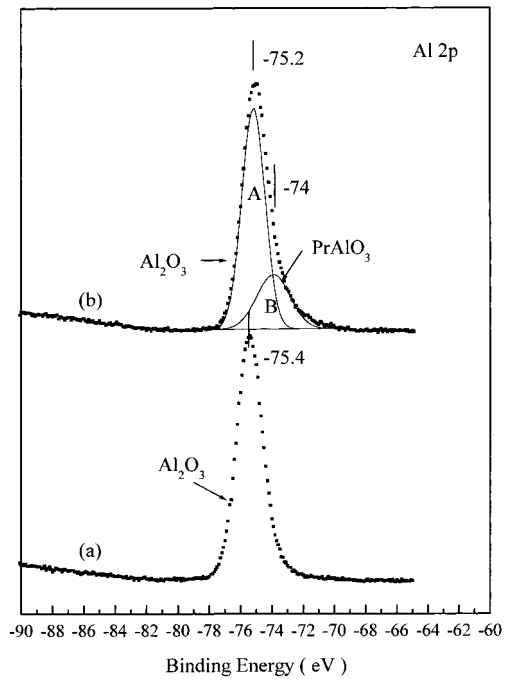

Figure 12. Al 2p XPS spectra of (a) Al_2O_3 and (b) Pr−O−Al films. Peaks A and B (1.98:1) located at −75.2 and −74 eV are assigned to Al_2O_3 and Pr−O−Al film, respectively.

Auger line. Further, the spectrum shows the Pr $3d_{5/2}$ and Pr $3d_{3/2}$ peaks due to the spin−orbit splitting.[57] The small peak denoted with s in the Pr 3d XPS spectrum of Pr_6O_{11} standard corresponds to PrO_2. The absence of this feature and the information gained from the XRD data (only $PrAlO_3$ phase) excludes the possibility of any tetravalent Pr species being present in the film material. The Nd 3d XPS spectra of the film and Nd_2O_3 standard show the characteristic Nd 3d features (Figure 13b). The tiny features located at −974 and −1010 eV are due to the oxygen 1s Auger lines. In summary, the ESCA (XPS) analysis reveals Pr and Nd to be present in their trivalent state.

Optical Properties. The refractive indices of the as-deposited films were determined by reflection ellipsometry which measures the modification of the polarization state of a linearly polarized light upon reflection from an optically active medium or a film covered surface. The complex ratio ρ was determined for the films deposited on silicon substrates.

$$\rho = r_{||}/r_{\perp} = \tan \psi^* e^{i\Delta}$$

where ψ and Δ are the amplitude ratio and the phase shift, respectively, of the parallel (||) and perpendicular ($\perp$) components and are generally given as tan ψ and cos Δ. The wavelength range for the determination of the refractive index "*n*" and the absorption coefficient "*k*" is 250−900 nm (Figure 14); however, the *n* and *k* values are considered only for the 400−850 nm region where the influence of the surface roughness (Figures 5 and 6) is rather negligible. The refractive indices calculated, using the Cauchy approximation model,[58] were found to be 1.76 and 1.67 for the Pr−O−Al and Nd−O−Al films, respectively, and are fairly constant in the range 400−900 nm. The relatively higher refractive indices suggest these films to be suitable for waveguide material.[43,44] The growth rates deduced from the film thickness calculated using the ellipsometric data were found to be approximately 1.7−1.8 μm/h.

The UV−Vis spectra of the as-deposited and annealed (900 °C) films are shown in Figure 15 which reveal the typical absorption features for Nd 4*f* intratransitions.[59] The observed peak positions are nearly the same in both cases, but due to the lack of ordering in the amorphous Nd−O−Al film the Stark structure is poorly resolved, resulting in broad peaks, typically observed in glass matrix.[60] The adjacent energy levels overlap and appear as a band in the spectrum (Figure 15). On the other hand, the annealed film shows the Stark components due to the crystal field splitting of Nd 4*f* levels. It may be mentioned that the absorption spectra of Nd^{3+} in different hosts are very similar, and the only effect of the host is to cause change in the relative peak intensities and the hyperfine splitting of the Stark levels.

Conclusions

The thermolytic transformation of **1** and **2** into oxide−oxide composites illustrates that the multicomponent

(57) Lütkehoff, S.; Neumann, M.; Slebarski, A. *Phys. Rev. B* **1995**, *52*, 13808.
(58) Azzam, R. M. A.; Bashara, N. M. *Ellipsometry and Polarized Light*; Elsevier: North-Holland, New York, 1977.
(59) Antic-Fidancev, E.; Lemaitre-Blaise, M.; Beaury, L.; Teste de Sagey; G.; Caro, P. *J. Chem. Phys.* **1980**, *73*, 4613. Rukmini, E.; Jayasankar, C. K. *Physica B* **1995**, *212*, 167.

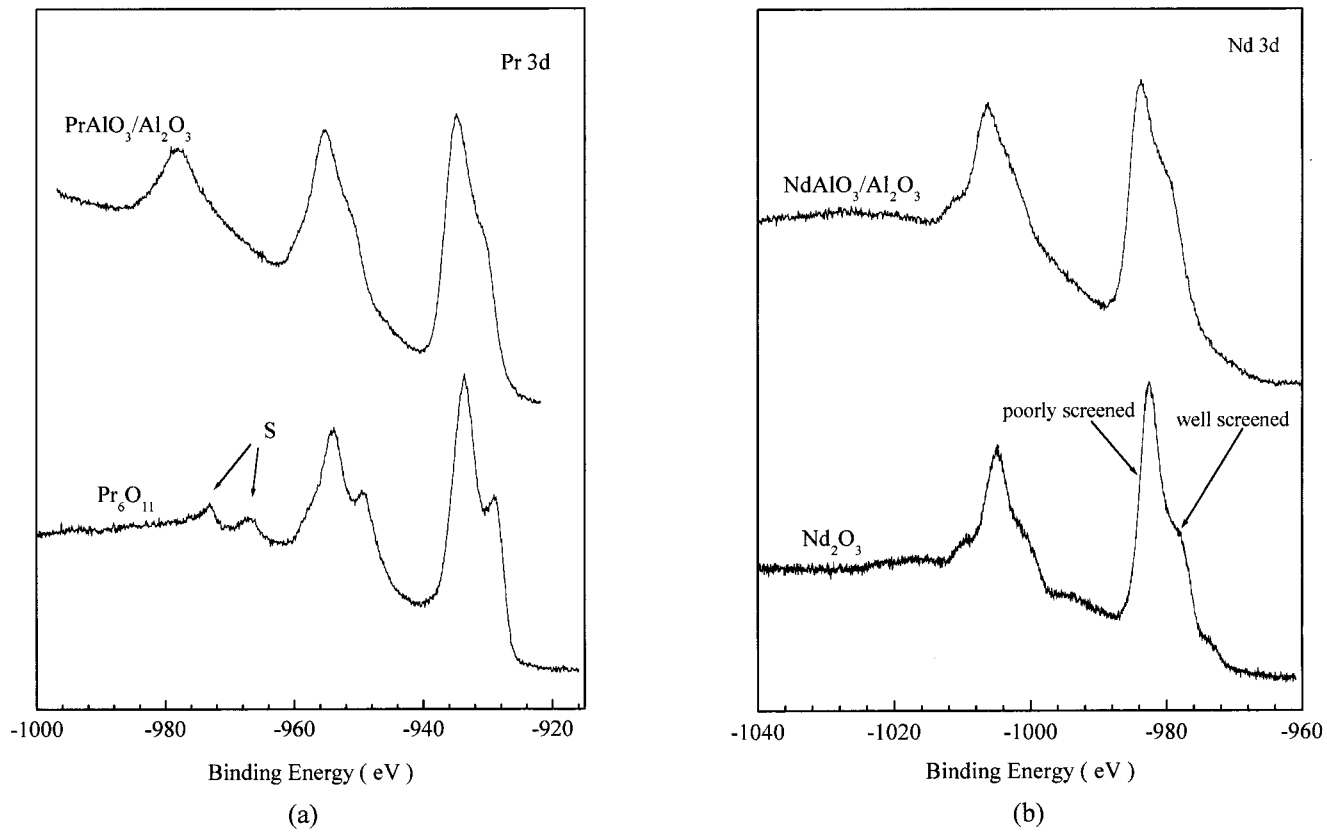

Figure 13. (a) Pr 3d XPS spectra of a Pr−O−Al film and Pr_6O_{11} reference sample and (b) Nd 3d XPS spectra of a Nd−O−Al film and Nd_2O_3.

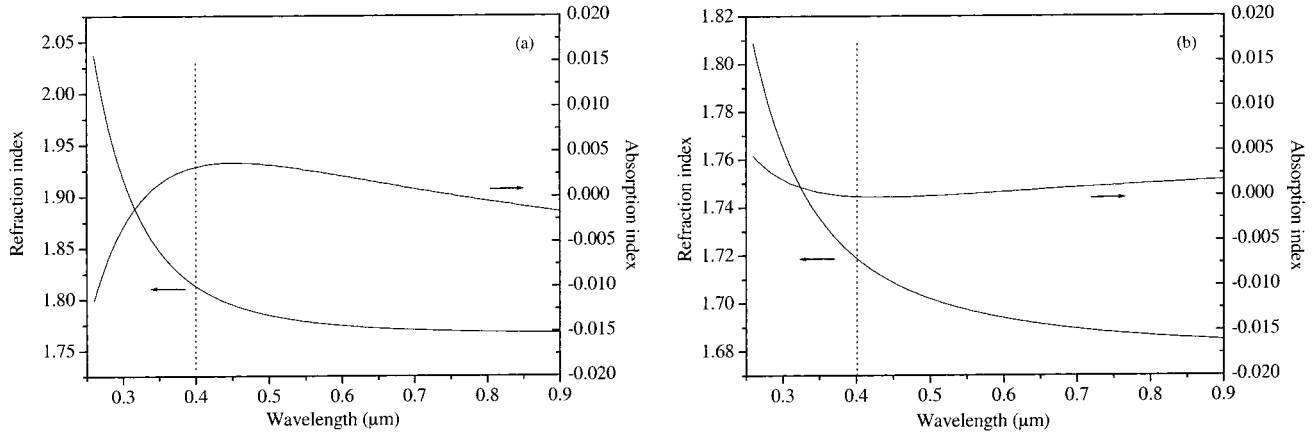

Figure 14. Refraction and absorption indices of (a) Pr−O−Al and (b) Nd−O−Al films.

thin films with unique nanostructures are accessible by a *single-source* CVD process. The preservation of the metal to metal ratio in the as-deposited films suggests a complete vapor transport of the precursor during the CVD process, invalidating the common doubt that the disparity in the volatilities of praseodymium (neodymium) and aluminum alkoxides may lead to the disproportionation of the mixed-metal frameworks. The CVD experiments suggest that Ln−O−Al bonds (Ln = Pr, Nd) remain intact during the precursor evaporation and decomposition giving a material of overall composition $LnAl_3O_6$, which forms a nanocomposite of $LnAlO_3$ and Al_2O_3 phases upon annealing. The selective phase separation into $LnAlO_3$ and amorphous alumina (a-Al_2O_3), nonformation of other Ln:Al:O stoichiometries (e.g., $Ln_3Al_5O_{12}$, $Ln_4Al_2O_9$, $LnAl_{13}O_{18}$) and preferential crystallization of $LnAlO_3$ upon annealing are probably driven by thermodynamics, for instance, the enthalpies of formation ($LnAlO_3$ vs ($Ln_3Al_5O_{12}$, $Ln_4Al_2O_9$, $LnAl_{13}O_{18}$) and Al_2O_3) and the specific heats of the two Gibbsian phases.[61] The low-temperature crystallization of $LnAlO_3$ phases and an enhanced stabilization of amorphous alumina phase indicate that the single-source precursors initially produce a homogeneous film with a −Al−O−Ln−O−Al− network and that the phase separation occurs upon annealing due to the difference in the diffusion coefficients in amorphous and crystalline solids. The segregation of individual metal oxides and formation of $LnAlO_3$ phase by a solid-state reaction between Nd_2O_3 and Al_2O_3 can be ruled out in the light

(60) Campbell, J. H.; Suratwala, T. I. *J. Non-Cryst. Solids* **2000**, *263−264*, 318.
(61) Wu, P.; Pelton, A. D. *J. Alloys Compd.* **1992**, *179*, 259.

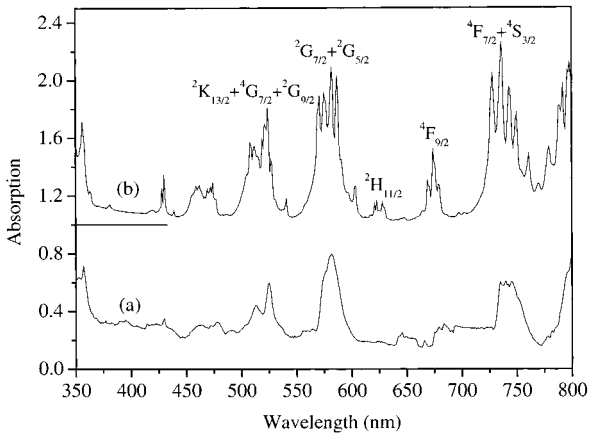

Figure 15. UV−Vis absorption spectra of (a) as-deposited Nd−O−Al film and (b) after annealing at 800 °C.

of various analyses used to characterize the surface-related and bulk properties of the films.

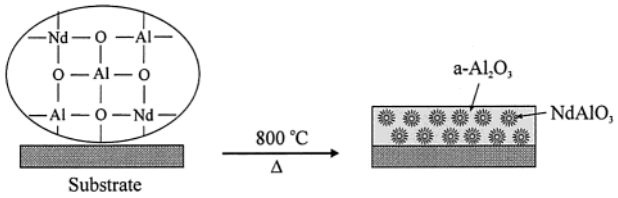

In contrast to the $PrAlO_3$ and $NdAlO_3$ phases, the delayed crystallization of alumina can be rationalized in terms of its lower heat capacity when compared with neodymium or praseodymium aluminate. Apparently, in the initial stages of heat treatment, the amorphous alumina allows the percolation of ions required for the grain growth of the $LnAlO_3$ phases. Owing to the difference in the heat capacities of the two phases, the nanocrystals of neodymium or praseodymium aluminate function as hot zones in the amorphous matrix and preferentially absorb the supplied thermal energy thereby further inhibiting the crystallization and grain growth of alumina particles. Finally, this work shows that the use of molecular precursors can lead to composite materials often not attainable by conventional processing methods. Since the characteristics of the endproduct are predetermined by the chemical nature of the precursor, the choice of starting material is crucial in such processes. The formation of a well-mixed biphasic material containing nanocrystallites of an optically active component embedded in an isotropic matrix allows to envisage interesting optical properties not anticipated in the individual phases. To verify our concept that isolation of individual $NdAlO_3$ grains in an alumina matrix can enhance the optical performance when compared to the bulk neodymium aluminate, we have studied the absorption and photoluminescence spectra of the two systems. The results show a noticeable enhancement in the optical properties of the composite system.[45]

Acknowledgment. The authors thank the Deutsche Forschungsgemeinschaft for providing the financial support in the framework of research program *Sonderforschungsbereich 277* at the Saarland University, Saarbruecken. We thank Dr. Michael Zimmer for recording the solid-state NMR spectra and Dr. Karsten Bartz for the GDMS analysis of the samples. The *Alexander von Humboldt* Foundation, Germany is gratefully acknowledged for a research fellowship to S.M. during 1994−6, when this work was initiated.

CM011092+